Experimental study of the shear flow effect on tidal turbine blade loading variation

Maëlys Magnier, Nina Delette, Philippe Druault, Benoît Gaurier, Grégory Germain

Renewable Energy
June 2022, Volume 193, Pages 744-757
https://doi.org/10.1016/j.renene.2022.05.042
https://archimer.ifremer.fr/doc/00772/88365/

Experimental study of the shear flow effect on tidal turbine blade loading variation

Magnier Maëlys [1, 2], Delette Nina [1], Druault Philippe [2], Gaurier Benoît [1], Germain Grégory [1, *]

[1] Ifremer, Marine Structure Laboratory, 150 Quai Gambetta, 62200, Boulogne sur Mer, France
[2] Sorbonne Université, CNRS, UMR 7190, Institut Jean Le Rond d'Alembert, F-75005, Paris, France

* Corresponding author : Grégory Germain, email address : gregory.germain@ifremer.fr

Abstract :

Tidal turbine arrays are planed to be installed in areas with strong currents where the flow can often be sheared throughout the water column. To study the shear flow effects on tidal turbine, four vertical velocity profiles are generated in a flume tank and are imposed to a three-bladed horizontal axis turbine model. Results show that the sheared velocity profiles do not impact the turbine average performance but are responsible for an increase of blade root streamwise load variations. Blade root streamwise load is moreover linked to the turbine rotational frequency and its harmonics. The velocity perceived by the blades during their rotation is estimated over the rotor area and is compared to the angular phase average of the streamwise load measured on the blades. The phase average of the load and the velocity perceived by the blades are highly correlated even if a varying phase lag has been noticed between these two quantities. This phase lag is dependent on the rotational speed of the turbine, on the incoming flow shear, and is probably caused by the turbine induction effects. This experimental study is a first step to understand the effect of shear velocity profiles on tidal turbines better.

Keywords : Marine renewable energies, Tidal turbine, Tidal velocity profiles, Inflow shear effects, Streamwise blade root loads, Angular phase average, Laser Doppler Velocimetry

1. Introduction

Each potential tidal area being unique, a lot of works has been carried out to characterize tidal current velocity profile and turbulence [20, 39, 29, 23, 11, 27]. This fine characterization of tidal stream properties is of key importance to evaluate the performance and lifetime of potential tidal turbines installed in these sites. Three main physical phenomena have to be taken into account: the turbulent intensity and the size of turbulent structures (the length scale) [5], the presence of waves at the surface [12], and the current velocity gradient over the water column [26].

The effects of turbulence on tidal turbines have been studied from many points of view. Mycek et al. [31] demonstrate that, even if averaged performance stays quite identical with or without turbulence, instantaneous behaviour fluctuates drastically when the turbulence intensity increases. The turbulence intensity has also a significant impact on the wake development [10]. A high level of turbulence makes the wake dissipates much faster than at low turbulence. For a high upstream turbulence intensity rate, the flow has almost recovered its upstream conditions, 6 diameters downstream from the turbine, in terms of velocity, turbulence intensity, and shear stress [31]. Gaurier et al. [18] and Druault and Germain [9] point out that large-scale turbulent structures, created by the interaction between a wide bathymetric obstacle and the flow, are strongly correlated to turbine loads and dominate its frequency response under 1 Hz. Thiébaut et al. [37] also show that large vertical scale eddies are responsible for a high-stress

regime of fatigue on the components of a tidal energy converter, reducing the lifetime of its components. The estimation of wave loading on tidal turbine has been investigated as well by [14, 7]. Results demonstrate that wave action induces large variations in turbine power and thrust compared to current only conditions. They concluded that the cyclic amplitude of loads is directly related to the wave conditions and that regular wave amplitude and frequency govern turbine wave-induced loads for both waves following or opposing the current.

The effects of shear flow on wind turbine have intensively been studied for several years. From these studies, is has been shown that the impact on the global turbine performance is limited. The blade loads are however significantly impacted and the performance evaluation is complicated [41, 36, 35, 24]. In the marine renewable energies field, only a few studies exist on this subject. Using CFD simulations, Mason-Jones et al. [26] focus on these specific effects and conclude that torque, power, and axial thrust, related to a chosen blade, have a cyclic behaviour in a highly shear flow. More precisely, they link the angular behaviour of the power to the velocity perceived by the blade. They conclude that the maximum power is shifted of an angle of $\approx 70°$ from the point where the blade should theoretically view the maximum of the velocity. They assume this difference comes from the induction effect of the turbine. Badshah et al. [3] come to the same conclusion, without any angular shift between the maximum power and the maximum velocity. They also study blade fatigue and deformation. From numerical results, Ke et al. [22] conclude that for a three-bladed horizontal axis turbine, the effect of a shear flow on turbine performance is small if the shear rate is small. On the contrary, when the shear increases, it becomes responsible for severe fluctuations of the device loading. Gaurier et al. [15, 18] study the impact on the blade loading of a shear and turbulent flow, generated by a wide bathymetric obstacle. Phase average loads show a dependency on the incoming shear velocity profile but, no link between loads variations and velocity variations could be established. Finally, Ahmed et al. [1] model the interaction between an inflow-shear and an horizontal-axis tidal turbine, accounting or not, for turbulence environment. They show that for both turbulent cases, the turbine rotor influences axial velocity and approach-flow turbulent structures about 1 D upstream to the rotor. The wake also extends beyond 10 D for both cases. The wake topology is slightly modified by the onset turbulence. That causes a small wake distortion and slightly aids the break-up of the vortex structures and makes the wake recovery slightly faster. When looking at phase-average load and surface pressure, being in realistic conditions only contributes to a small component of the overall load fluctuation. Vinod et al. [40] mimic sheared-turbulent inflow with the use of an active-grid turbulence generator in a 0.61 m x 0.61 m test section water tunnel. They found an increase of $\approx 30\%$ in torque fluctuations on a $\approx 0.3\ m$ diameter rotor for sheared inflow.

The purpose of this paper is thus to investigate the impact of vertical shear velocity profiles on both the estimation of tidal turbine performance and the loads experienced by the blades. To carry out this study, four incoming velocity profiles are generated in an 8 m^2 section flume tank using a grid arrangement. A three-bladed horizontal axis tidal turbine of 1 MW capacity, at scale 1:20, is set in these shear flows and its behaviour, e.g. performance and blade loads, is studied. In this work, the turbulent intensity is kept low in order to only focus on the shear-inflow effects. The aim of this paper is to identify the blade load variations accounting for the shear velocity effect only.

After a short description of the experimental setup, incoming velocity profiles are presented. Then, the focus is done on the evaluation of the turbine power coefficient, strongly dependent on the velocity chosen for its estimation. Next, blades' streamwise load behaviours are analysed in a temporal and spectral point of view, as well as versus the angular position of the rotor. Finally, phase averaged blade loads are compared to velocity perceived by the blade during its rotation. Similarities and differences between phase average loads and blade apparent velocity

are commented and a deeper analysis is proposed.

2. Experimental set-up and inflow characteristics

2.1. Flume tank and tidal turbine prototype

The tests have been carried out in the wave and current circulating tank of IFREMER, in Boulogne-sur-Mer (France) presented in Figure 1. The test section is 18 m long, 4 m wide and 2 m deep. The tank is equipped with two pumps which set the 700 m^3 of water in motion to generate current up to 2.2 m/s [16]. In this work, the velocity can be separated into three components denoted (U, V, W) along the $(\overrightarrow{x}, \overrightarrow{y}, \overrightarrow{z})$ directions respectively. The x-axis is the main flow direction, the y-axis is oriented from the observation windows towards the wall, and the z-axis is directed from the tank bottom to the free surface (see Figure 4). Each velocity component is separated according to the Reynolds decomposition as follows: $U(x, y, z, t) = \overline{U}(x, y, z) + u'(x, y, z, t)$, where $\overline{U}$ is the temporal mean value of U and u' is its fluctuating part.

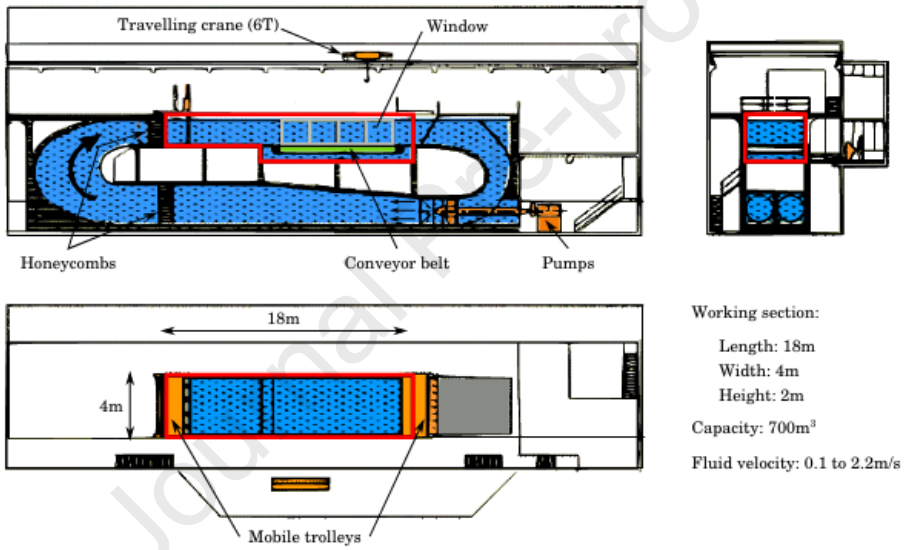

Figure 1: Schematic view of the IFREMER flume tank.

The flume tank is equipped with a grid and a honeycomb structure to homogenize the inflow and control the turbulence. Thanks to these structures, $\overline{U}$ remains constant over the tank height, with an almost uniform vertical velocity profile. However, this velocity profile significantly differs from *in-situ* ones, since the bathymetry induced velocity shear is absent in the tank. It is also the case from the turbine rotor point of view. To recreate velocity profiles corresponding to what is observed *in-situ*, three *"Panels"* have been designed [30, 25]. These *Panels* are made of multiple layers of wire meshes (Figure 2). The non-uniformity of layers distribution along the z-axis generates a vertically sheared velocity profile, like those used in wind tunnels [32]. Thanks to the grid and meshes arrangement presented in Figure 2, each *Panel* provides a different sheared velocity profile. Including the *Original grid* case, four case studies are thus created with the corresponding velocity profiles described in part 2.2.

To evaluate the shear effect of velocity profiles on tidal stream turbines, a 1:20 scale three-bladed horizontal axis turbine of 1 MW capacity, is used (Figure 3). The rotor of diameter $D = 2R = 0.724$ m is composed of three 307 mm long blades made in carbon fibre which follow a NACA $63-418$ profile [17]. The turbine is equipped with a motor driven by a controller. A slipring is moreover connected to the axis and allows to transfer the signals from the different

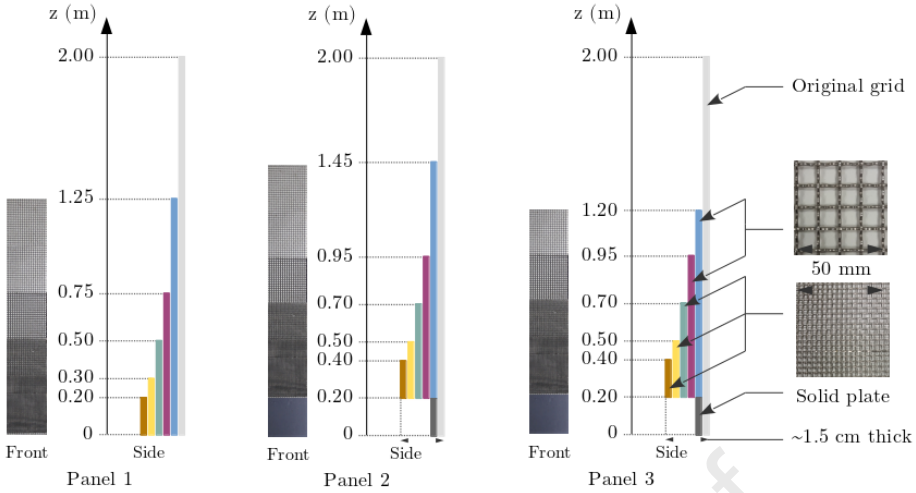

Figure 2: Grids and meshes arrangement, named *Panel 1* to 3, for generation of realistic sheared velocity profiles. Coarse mesh is made with 2 mm thickness wires evenly-spaced every 10 mm. Fine mesh is made with 0.7 mm thickness wires evenly-spaced every 2 mm.

rotating sensors present on the rotor. These signals then go up into the stanchion to the surface.

Each turbine's blade root is equipped with load-cells which measure two forces (F_x and F_y) and three moments (M_x, M_y, and M_z), as detailed in Figure 3. A rotating cartesian coordinate system $(\overrightarrow{e_x}, \overrightarrow{e_y}, \overrightarrow{e_z})$ is associated with each blade root. The global rotor torque and thrust are also measured by a specific instrumentation. The uncertainty of measurement is 0.2% for the loads and 0.04 tr/min for the rotational speed, according to the manufacturer. Since the turbine's rotor is not equipped with angular position sensor, we made the hypothesis that this angular position can be processed through the blade F_y measurements, as previously done in Gaurier et al. [18]. This idea is based on the fact that the blade weight is projected on the $\overrightarrow{e_y}$ direction for every time step. The complete processing is described in the following three steps procedure:

1. The fluctuating parts of the F_y signals are first extracted for each blade.
2. They are then filtered with a band-pass filter around the rotation frequency f_r. This step enables the weight component of the blade to be kept only. This constitutes the main hypothesis of this method: the blades' weight only responds at the rotation frequency and no other physical perturbation affects the F_y signals at the rotation frequency.
3. Using the phase of these sinusoidal signals, we get the three θ_i angles corresponding to the three blades. Then, we defined a convention: the main rotor angle is defined with $\theta = 0$ rad corresponds to blade 1 at the top dead centre. This main rotor angle is the average of the three θ_i (re-phased for blade 2 and 3, with $\pm 2\pi/3$ rad). The average is only processed if the difference between the three re-phased θ_i is lower than a given threshold.

A possible uncertainty source concerning this method is the temporal precision: when the turbine rotation speed is set to the designed tip speed ratio, the blade rotation is 5° between each time step, which can lead to an error of 2.5°.

To evaluate the impact of shear velocity profile on the turbine behaviour, the turbine is positioned 12.5 m downstream of the panels' assembly and the honeycomb structure. The rotor is set in the centre of the test section, with the turbine hub at $(y, z) = (2\text{ m}, 1\text{ m})$, as presented in Figure 4.

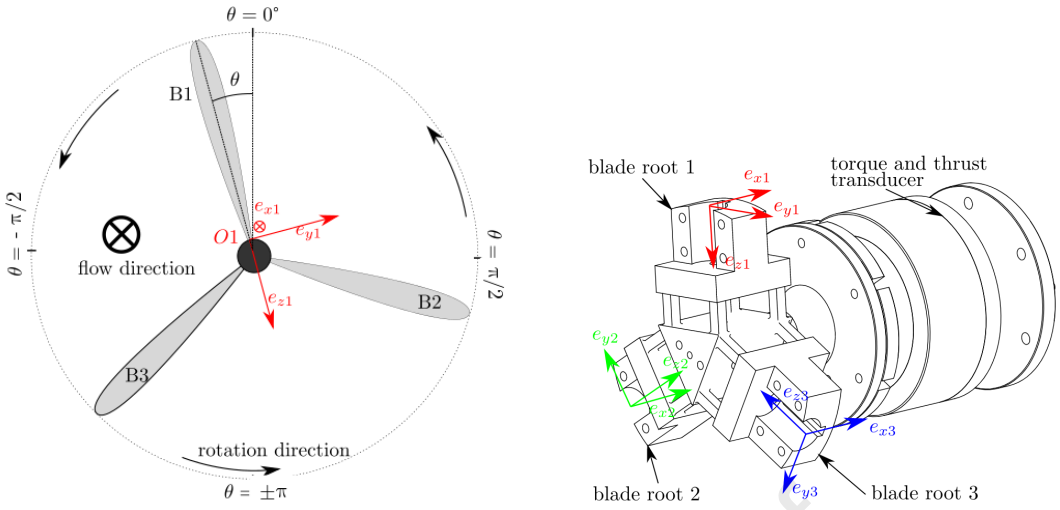

Figure 3: Blade axis and rotation direction of the turbine (*left*) and blade roots and torque Q and thrust T transducer (*right*).

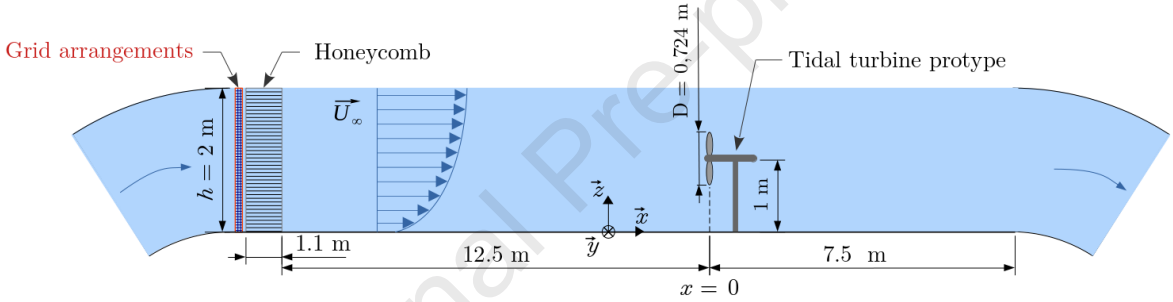

Figure 4: Schematic view of the experimental set-up, with the turbine fixed 12.5 m downstream the honeycomb outlet.

2.2. Incoming vertical velocity profiles characterization

The incoming flow is assumed to be steady and constant, with the imposed velocity: $U_\infty = 1$ m/s and $V_\infty = W_\infty = 0$ m/s. To characterize incident velocity profiles, a 3 Components Laser Doppler Velocimetry system (3C LDV) is used. Before measurements, the tank is seeded with 10 μm diameter silver coated glass micro-particles. 3C LDV sampling frequency depends on the number of particles viewed by the sensor of the probe during the measurement. The LDV acquisition frequency is higher than 100 Hz for the three components of the data used in this study.

According to the 3C LDV measurements, we established that V and W are always smaller than 0.02 m/s on the study region. For the four study cases, V and W are thus neglected in the rotor plane. In the following, the study is consequently focused on the streamwise component U of the velocity only. To characterise the velocity profile along the tank height, measurements are carried out every 5 to 20 cm, depending on the degree of precision required to capture the variation of U. On each measurement point, the acquisition lasts 180 s. The obtained velocity profiles $\overline{U(z)}$ are presented in Figure 5. The standard deviation of $U(z,t)$, denoted $\sigma(U(z))$, is presented in the same figure to highlight the fluctuating part of the flow.

As expected, the *Original grid* generates an almost uniform velocity profile over the tank. On the contrary, the *Panel 3* velocity profile presents a strong velocity gradient throughout the water column. Nevertheless, *Panels 1* and *2* create more complicated velocity profiles

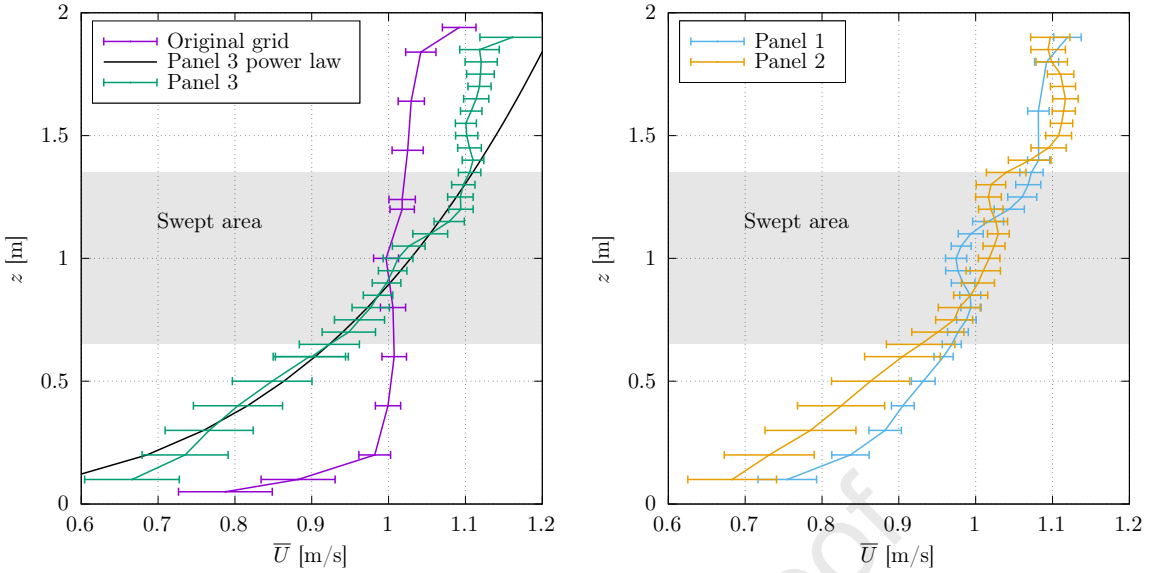

Figure 5: Vertical profiles of the streamwise velocity $\overline{U(z)}$ obtained for the *Panels* describes in Figure 2. Data come from 3C LDV measurements in the rotor plane for the four cases. Error bar represents standard deviation $\sigma(U(z))$. The grey shaded zone materializes the area covered by the turbine blade. *Panel 3* power-law coefficient: $\alpha = 4$ and $U_0 = 1.23$ m/s (see equation 1).

because they both present a low-velocity zone in the swept area. For *Panel 1*, this zone is located around $z = 1$ m while it is around $z = 1.3$ m for *Panel 2*.

At sea, the current velocity profile is usually non-linear as well. These profiles show multiple slopes depending on the site, the tidal range, the direction of the flow, and the wave conditions. Their velocity gradients are thus not constant along the depth. One way to define their slope is to use power-laws, enabling the profiles to be compared using a unique coefficient α. $U_{PowerLaw}(z)$ is defined as:

$$U_{PowerLaw}(z) = U_{ref} \times \left(\frac{z}{D_e}\right)^{1/\alpha} \tag{1}$$

with U_{ref} corresponding to the surface velocity (or velocity at mean depth), D_e represents the depth of the water column and z is the distance from the bottom. In the Alderney Race (France), a large study has been carried out, using towed ADCP [34]. During this survey, the waves' effects have been neglected by the authors. They found current velocity profiles following equation 1, with α between 4 and 14. A trend stands however out: the power-law corresponding to $\alpha = 7$ is representative of many marine renewable energy sites [11, 20, 38, 23]. To link our case to what is encountered *in-situ*, we determine the power-law that best fits the *Panel 3* velocity profile over the rotor height. It gives the following parameters: $U_{ref} = 1.23$ m/s, and $\alpha = 4$. This curve is plotted in Figure 5. The obtained coefficient α is in the range of the Alderney Race and provides the most sheared possible case. The shear velocity profile generated by *Panel 3* is thus representative of *in-situ* vertical velocity profile. Additionally, the *Panel 1* case and the *Panel 2* case, which generate complex velocity profiles, correspond to more specific *in-situ* cases, caused by site-specificity.

The introduction of the *Panels* may furthermore generate turbulence, which can be quantified by the 1D turbulence intensity I_{1D}:

$$I_{1D} = \frac{\sigma(U)}{\overline{U}} \tag{2}$$

Turbulence intensity over the tank height for the four cases is plotted in Figure 6. Turbulence intensity ranges from 1% to 3% over the rotor height, for *Original grid* and *Panel 1* cases. It reaches 3.5% in the bottom part of the rotor for the *Panels 2* and *3* cases. This is due to the solid plate used at the very bottom part of the grid and meshes arrangement, which strongly reduces the averaged velocity in this area and acts as a backward-facing step avoiding the flow to go through the last rows of the honeycomb structure.

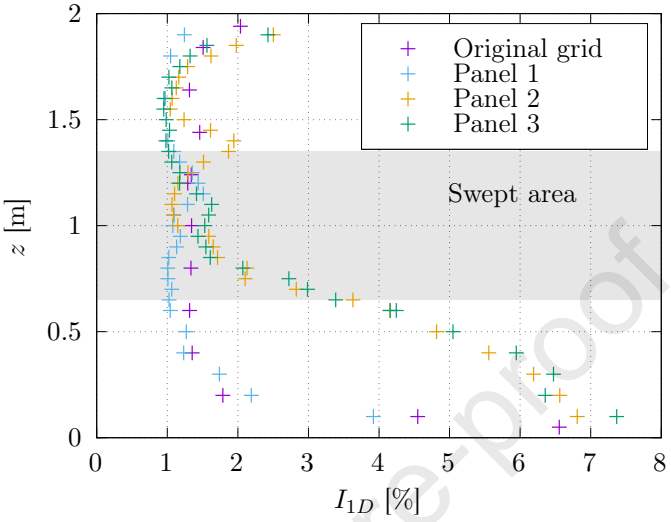

Figure 6: Turbulence intensity I_{1D} over the water column for the four cases.

To complete the characterisation of the four velocity profiles over the rotor height, their mean velocity, mean 1D turbulent intensity, and maximum mean velocity difference $\Delta_{max}\overline{U}$ are gathered in table 1. With the use of the *Panels*, three shear velocity profiles have been generated, while the *Original grid* provides a uniform profile over the rotor height. Moreover, for all cases, the mean velocity on the rotor area is the same and the turbulence intensity is low: $\widehat{\overline{U}} = 1.0$ m/s and $\widehat{I_{1D}} \leq 2.5\%$, with $\overline{\square}$ the temporal average and $\widehat{\square}$ the spatial average over the rotor area of the turbine.

In the following, we will consequently focus on the effect of the shear on the turbine only. In the next section, the turbine response to these velocity profiles is studied and compared between cases.

Case	$\widehat{\overline{U}}$ [m/s]	$\Delta_{max}\overline{U}$ [m/s]	$\widehat{I_{1D}}$ [%]
Original grid	1.00	0.01	1.6
Panel 1	1.01	0.10	1.5
Panel 2	1.01	0.11	2.5
Panel 3	1.02	0.18	2.5

Table 1: Mean velocity, 1D turbulent intensity, and maximum velocity difference over the rotor height.

3. Shear flow effect on a tidal turbine

3.1. Effect on turbine global performance

In this section, the global tidal turbine performance is analysed and compared between the cases. A relevant criterion to quantify the turbine performance is the power coefficient C_p,

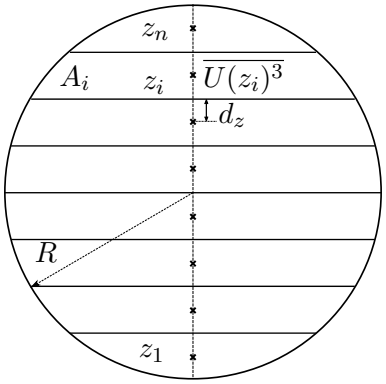

Figure 7: Methodology to obtain $\widehat{\overline{U^3}}$, the mean value of $\overline{U^3}$ over the swept area. In our calculation, $n = 16$, $dz = 0.025$ m.

which is defined as:

$$C_p = \frac{\overline{Q}\overline{\omega}}{\frac{1}{2}\rho A \widehat{\overline{U^3}}} \tag{3}$$

with A the area swept by the blades ($A = \pi R^2$), $\overline{\omega}$ the rotational speed of the turbine and ρ the water density. $\overline{Q}$ is the rotor mean torque measured on the rotation axis and $\widehat{\overline{U^3}}$ is the mean flow velocity view by the turbine, calculated as follow:

$$\widehat{\overline{U^3}} = \frac{1}{A}\sum_{i=1}^{n} \overline{U(z_i)^3} A_i \tag{4}$$

with z_i the i^{th} slice where the velocity is considered as constant and A_i its area ($A = \sum_{i=1}^{n} A_i$). n is the number of slices used for the calculation. The number of slices is strongly dependent on the case-study. In our case, the value of $\widehat{\overline{U}}$, $\widehat{\overline{U^2}}$ and $\widehat{\overline{U^3}}$ are not significantly modified ($< 10^{-3}$) for $n \geq 12$, corresponding to a slice interval of 6.0 cm. In this study, $n = 16$. This equivalent velocity has been used before the C_p or kinetic energy calculations in wind shear cases, e.g. by [42, 2] and is imposed by IEC norms for tidal turbine [21]. To use this method, $\overline{U}$ is assumed to be constant along the y-axis. Thus, using the velocity profiles established in part 2.2, $\overline{U(z_i)^3}$ is known at each height z_i and assume to be constant over the i^{th} slice. Please note that the cubing of velocity should be calculated before temporal and spatial averaging to obtain a correct C_p as explained by [5]. A schematic of the $\widehat{\overline{U^3}}$ calculation method is presented in Figure 7.

In Figure 8, performance coefficients are plotted versus the TSR (Tip Speed Ratio) for the four cases. The TSR corresponds to a normalised rotational speed and is defined as follow: $TSR = \overline{\omega}R/\widehat{\overline{U}}$. At first sight, the behaviour of C_p is the same whatever the shear with small fluctuations ($< 5\%$ of the mean value). For the highest sheared case, the C_p is slightly reduced (5%). The thrust coefficient shows an expected behavior, increasing with the TSR. For the *Original grid*, *Panel 1* and *Panel 2* cases, the thrust coefficient is similar. The C_t obtained for Panel 3 case is a bit lower. These observations are the same than the one already observed for the C_p curve. The standard deviation of C_p and C_t coefficients also show similar trends. They represent less than 5% of the mean value and slightly increase with the TSR, as presented in Gaurier et al. [19] for the same turbine model. The only exception is for $TSR = 2.5$, where the standard-deviation of the C_p coefficient presents a steep gradient. At this point, the controller of the turbine has difficulties to regulate the rotation speed of the turbine, causing

thus higher standard deviation value for all *Panel* cases. Finally, the presence of a vertical velocity gradient does not impact the mean turbine behaviour, as seen in Vinod et al. [40].

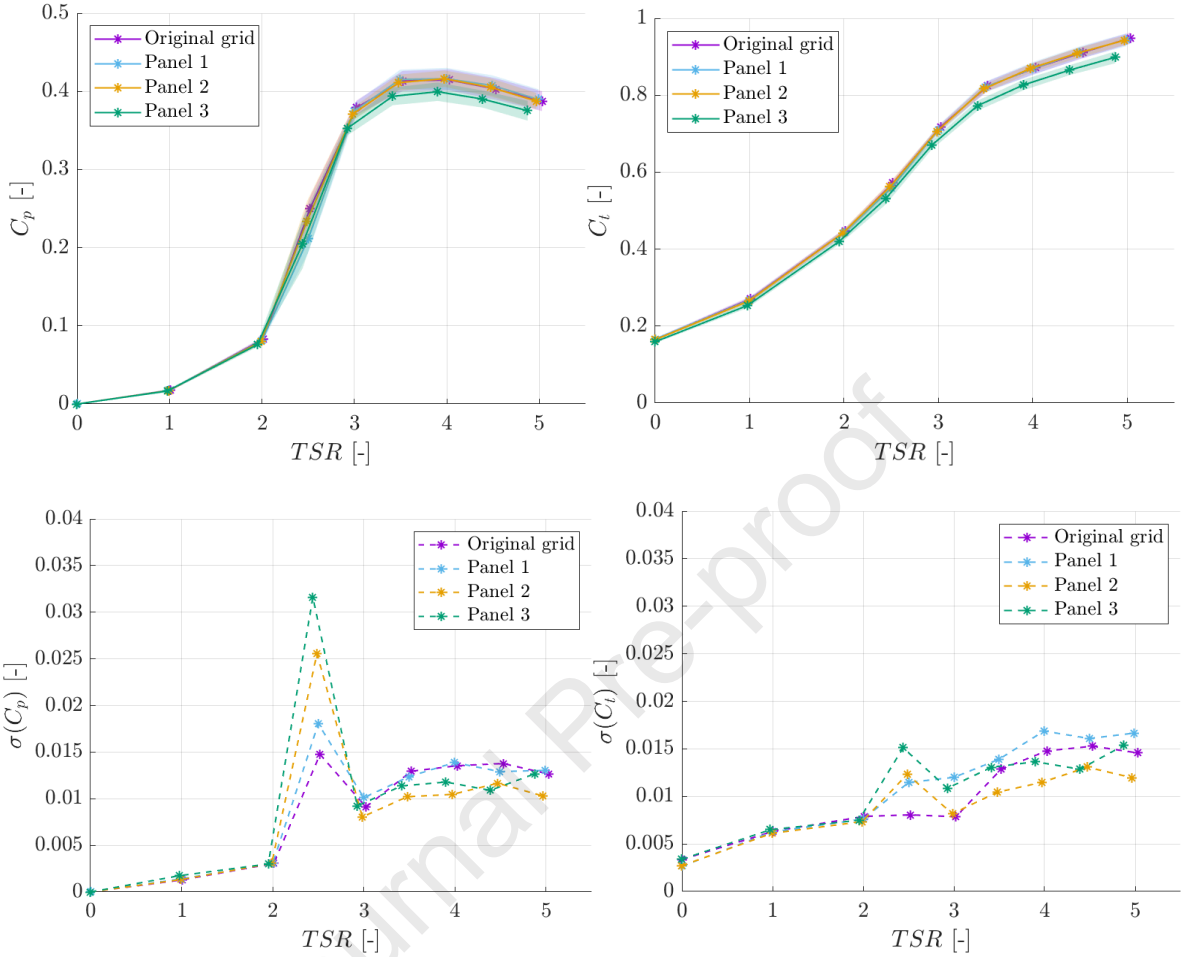

Figure 8: Power curves for the four cases. Top line: Power coefficient C_p (left) and thrust coefficient C_t (right). The shaded areas represent their standard deviation. Bottom line: Standard deviation of C_p (left) and of C_t (right).

This conclusion depends on the choice of the characteristic velocity, as shown in table 2. This remark shows the importance of using velocity over the entire swept area $\widehat{\overline{U^3}}$ and $\widehat{\overline{U}}$ instead of its value at the rotor centre height only. As the velocity gradient is not constant, $\overline{U(z = 1\text{ m})}$ is not representative of the velocity perceived by the blades. For example, taking the *Panel 1* case, the low-velocity zone at $z = 1$ m leads to an underestimation of the velocity seen by the blades. For our cases, if $\overline{U(z = 1\text{ m})}$ is considered for the C_p calculation, the difference on C_p values would be in the range 3% to 7%. These relative differences are summed up in Table 2. According to these results, the obtained values of C_p are more impacted by the way it is calculated than by the presence of a vertical velocity shear. The calculation of the C_p coefficient has thus to be made very cautiously: the specificities of the velocity perceived by the turbine, e.g. shear inflow, play a decisive role. Accounting for these specificities, the C_p coefficient enables the real turbine performance to be calculated. Finally, it shows that if the incoming velocity average over the rotor area is the same, the shear does not affect the turbine mean performance, as previously demonstrated for wind turbine [2, 42].

Case	C_p at $TSR4$, calculated with $\overline{U(z=1\text{m})}$	C_p at $TSR4$, calculated with $\widehat{\overline{U}}$	Difference of C_p for $TSR \in [3.5:5]$
Ori. grid	0.42	0.41	3%
Panel 1	0.45	0.42	7%
Panel 2	0.40	0.42	4%
Panel 3	0.42	0.40	5%

Table 2: Relative differences on C_p depending on how the cubed velocity is chosen.

3.2. Effect on blade loadings

Although velocity shear does not change global turbine performance, it may impact the instantaneous behaviour, especially the variation of blade loadings. In this part, the focus is done on blade 1 (see Figure 3), knowing that the results are equivalent for the three blades. The turbine is studied at its operating point $TSR = 4$. The acquisition of F_{x1} lasts 180 s. This time is required to obtain a converged mean value. In Figure 9, the fluctuating part F'_{x1} is plotted and some periodic variations are seen with smaller fluctuations due to other flow variations. To quantify F_{x1} over the entire acquisition duration, the mean value and its variations are summed up, for the four cases, in Table 3. It appears that both mean values and variations are bigger for the *Panel 3* case, while *Panel 1* and *Panel 2* cases present similar behaviours. The shear induced by *Panel 3* seems to have a more pronounced impact than the two other cases. Thus, the incoming shear velocity profile has a greater influence on blade load than on global performance C_p.

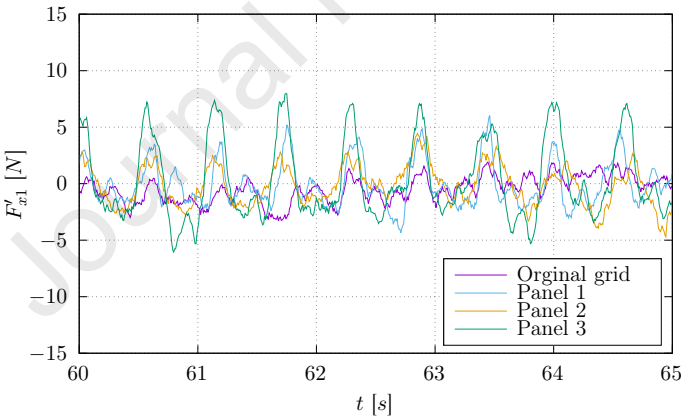

Figure 9: Evolution of the blade 1 load fluctuating part F'_{x1} with the time, between 60 s and 65 s, when the turbine rotates at $TSR = 4$. For more readability of the figure, $F'_{x1}(t)$ signals have been re-phase using phase lag from cross-correlation presented in table 5.

Case	$\overline{F_{x1}}$	$\sigma(F_{x1})/\overline{F_{x1}}$ [%]
Original grid	55.7 N	2.2%
Panel 1	56.9 N	3.5%
Panel 2	57.0 N	3.6%
Panel 3	59.7 N	6.2%

Table 3: Mean load and proportion of the standard deviation.

To investigate the spectral behaviour of the load F_{x1}, a Fast Fourier Transform (FFT)

analysis is conducted. On the FFT decomposition presented in Figure 10, there is a peak at the frequency 1.8 Hz for the *Panel 1*, *2*, and *3* cases. This frequency corresponds to the blade passing frequency f_r. The peak amplitude is more important in the *Panel 3* case: the magnitude of the variation is higher and reaches 4 N while it is less than 2 N in other cases. Moreover, in the *Original grid* case and the *Panel 1* case, a peak appears at the first sub-harmonic ($2 \times f_r$) of the blade rotation frequency. It is the signature, in the frequency domain, of the low velocity zone centred at $z \approx 1$ m, where the blades pass twice per revolution, at $\theta \approx \pi/2$ and at $\theta \approx -\pi/2$. In *Panel 2* and *Panel 3* cases, this low velocity zone is not present and the peak at $2 \times f_r$ is significantly smaller than the one at f_r, on the contrary to the two other cases where $F_{x1}(2f_r) > F_{x1}(f_r)$. A phenomenon at $2 \times f_r$ also appears in *Panel 3* case but it is less pronounced than at f_r. Finally, a frequency peak appears at $3 \times f_r$ in *Panel 1* case, quite as high as the peaks at f_r and $2 \times f_r$, coming from global tri-bladed rotor effects. Thus, the impact of the velocity profile is visible on the spectrum since it changes the emerging frequency and magnitude of spectrum peaks.

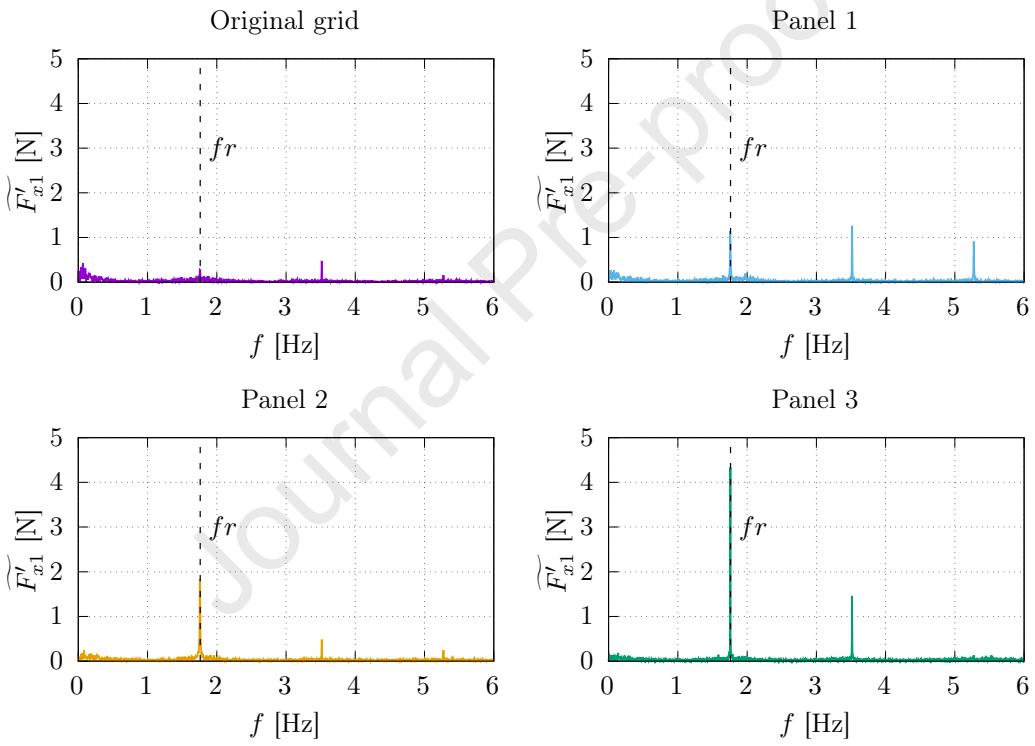

Figure 10: Fast Fourier Transform (FFT) of the local load fluctuating part F'_{x1} when the blade rotates at $TSR = 4$.

F_{x1} spectra have shown that load variations are linked to the turbine rotation. It is then interesting to relate the streamwise load variation of blade 1 to its angular position. A scatter plot is obtained and can be interpolated to calculate the angular phase average $\mathcal{F}_{x1}(\theta)$, for each discretized angular position. This phase average $\mathcal{F}_{x1}(\theta)$ is presented in Figure 11. In the following, $\mathcal{F}_x$ and $\mathcal{U}$ represent the angular phase average of the corresponding quantities and are only dependent on the angular position θ of the rotor.

For the *Original grid* case, $\mathcal{F}_{x1}(\theta)$ is nearly independent on θ. For the three other cases, $\mathcal{F}_{x1}(\theta)$ varies with the blade angular position: shear velocity profiles impact the phase average of the streamwise load. For *Panels 1* and *3* cases, $\mathcal{F}_{x1}(\theta)$ presents a maximum at $\theta \approx -\pi/4$, which is particularly significant for *Panel 3* case. In fact, this maximum appears just after (in

the rotational direction) the position where the blade is at the top dead centre ($\theta = 0$ rad), i.e. where $\overline{U}$ is maximal. The phase average of the streamwise load $\mathcal{F}_{x1}$ obtained for *Panel 1* and *3* cases are similar, even if the magnitude of the angular variation is smaller than in *Panel 1* case. Result obtained for the *Panel 2* case is relatively different from the other cases, with a lower maximum value, which is positioned at $\theta = 0$ rad.

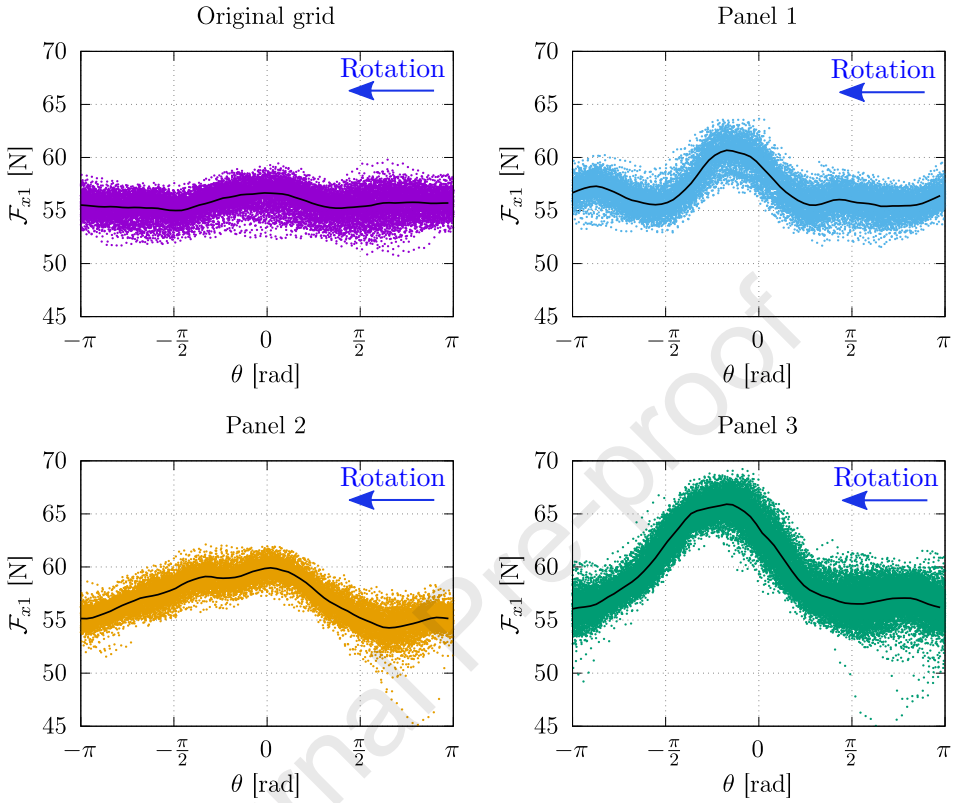

Figure 11: Angular repartition of blade 1 load F_{x1} measurement points (in N) when the turbine rotates at $TSR = 4$. The solid line represents its phase average $\mathcal{F}_{x1}(\theta)$. The direction of rotation is indicated by the blue arrow and corresponds to a negative direction.

According to these presented results, when the velocity profile is sheared, the link between the blade passing frequency and the phase average streamwise load is more pronounced. Globally, it appears that $\mathcal{F}_{x1}(\theta)$ is maximum near $\theta = 0$ rad and minimum at $\theta = -\pi$ rad, when the velocity reaches the corresponding extrema. In the following, the blade streamwise loads are phase averaged and analysed.

3.3. Angular correlation between velocity and load variation

In the previous section, the temporal and angular variations of the blade loading have been analysed, for the four cases. This highlights the link between streamwise loads and streamwise velocity which can be expressed as [4, 6, 8]:

$$F_{tot}(t) = KU^2(t) \tag{5}$$

where K is assumed to be constant. Using the Reynolds' decomposition, equation 5 becomes:

$$F_{tot}(t) = K(\overline{U} + u'(t))^2 \tag{6}$$

$$F_{tot}(t) = K(\overline{U}^2 + 2\overline{U}u'(t) + u'^2(t)) \tag{7}$$

As measurements are not synchronised, only the time average of the equation is kept:

$$\overline{F_{tot}} = K(\overline{U}^2 + \overline{u'^2}) \tag{8}$$

Moreover, it was shown in part 2.2 that $\sqrt{\overline{u'^2}}$ represents less than 4% of $\overline{U}$, and can be neglected:

$$\overline{F_{tot}} \approx K\overline{U}^2 \tag{9}$$

From that point and as done in the previous section, the focus is made on blade 1 only. Results are however similar for blades 2 and 3. The load-cell which measures the streamwise component of the load F_{x1} measures the integrated pressure exercised by the flow over the blade's surface, from the foot to the tip. This load is thus linked to the variation of the perceived velocity which depends on the angular position of the blade θ. Mathematically, the velocity perceived by the blade $\mathcal{U}(\theta)$ is defined as the time average velocity $\overline{U}$ from LDV measurements integrated on the blade surface, depending on its position θ. To stay consistent with phase average velocity $\mathcal{U}(\theta)$ perceived by blades, the blade streamwise load has to be a phase average: $\mathcal{F}_{x1}(\theta)$. Equation 9 thus becomes:

$$\mathcal{F}_{x1}(\theta) \approx K\mathcal{U}^2(\theta) \tag{10}$$

This mathematical link is experimentally studied in the following, to explain the impact of angular velocity variations on the blade load during the rotation.

3.3.1. Angular velocity perceived by the blade calculation

To compare the streamwise blade phase average load $\mathcal{F}_{x1}(\theta)$ to the squared velocity perceived by the blade $\mathcal{U}^2(\theta)$, this velocity has to be calculated first. LDV measurements have been done over the tank height to obtain time averaged velocity as plotted in Figure 5. The velocity is supposed to be constant along the y-axis, thus a 2D velocity cartography is obtained on the rotor plane by extruding the vertical velocity profile (interpolated along z-axis) along y-axis as plotted in Figure 12. From this part, we choose the turbine rotation axis as origin of the coordinate system.

The blade rotation angle is noted θ in the following (see Figure 13). Then, polar coordinates are used. $\overline{U(r,\theta)} = \overline{U(z)}$ is the velocity in this coordinates system, with $z = r\cos(\theta)$. $\overline{U(r,\theta)}$ is not dependent on y because the assumption has been done that the velocity is constant over y-axis.

To calculate the velocity $\mathcal{U}(\theta)$ perceived by the blade on a revolution, the blade is assumed to be linear, with zero thickness (red dashed line in Figure 13). Note that we compared the velocity calculated from the blade surface to the velocity calculated from the blade central line (retain calculation) and that the obtained velocity is almost equal. With these approximations, the velocity perceived by the blade is expressed as:

$$\mathcal{U}(\theta) = \frac{1}{R}\int_0^R \overline{U(r,\theta)}\,\mathrm{d}r \tag{11}$$

To numerically calculate $\mathcal{U}(\theta)$, the space is discretised. In cartesian coordinates,$z = z_1 + d_z n_z$ with $z_1 = -0.35$ m. In polar coordinates, $\theta = -\pi + d_\theta n_\theta$ and $r = d_r n_r$, $R = d_r N_r$. The velocity integrated on the blade thus becomes:

$$\mathcal{U}[n_\theta] = \frac{1}{N_r}\sum_{n_r=1}^{N_r} \overline{U[n_r, n_\theta]} \tag{12}$$

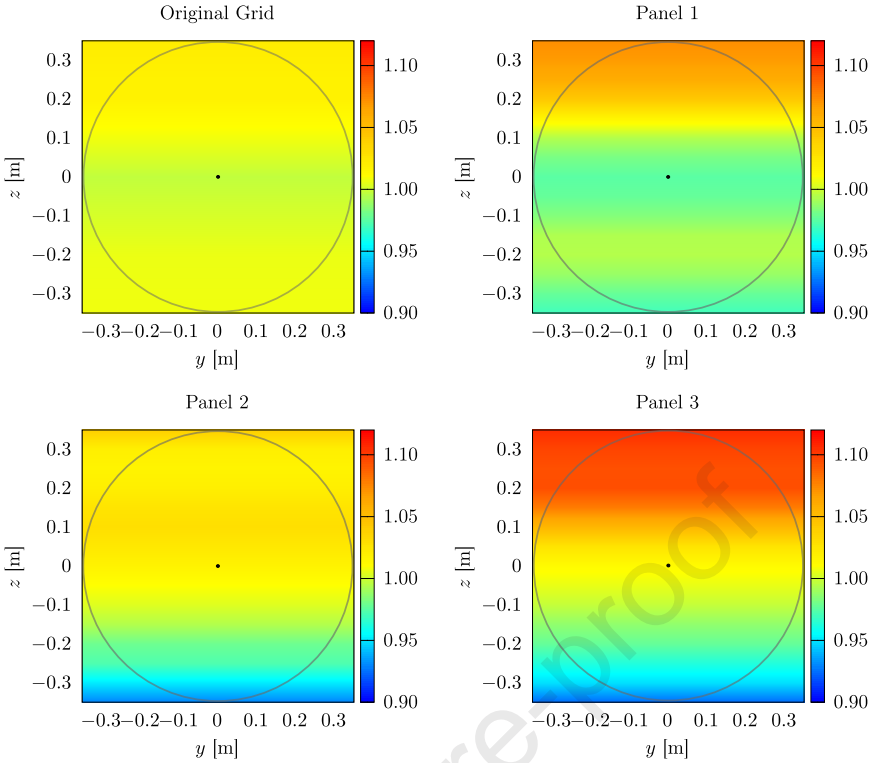

Figure 12: Cartography of $\overline{U}(z)$ on the the swept area in the four cases. Note that the origin of the coordinate system move to the centre of the turbine for more simplicity.

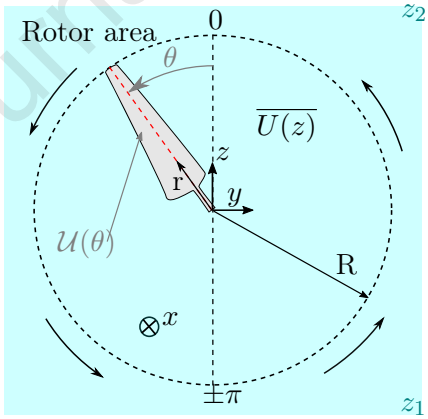

Figure 13: Definition of the notation used to calculate the velocity perceived by the blade.

The incoming velocity in the rotor plane have also to be discretised as function of cartesian and polar coordinates.

$$\overline{U[n_z]} = \overline{U(z_1 + d_z n_z)}$$

$$\overline{U[n_r, n_\theta]} = \overline{U(d_r n_r - \pi + d_\theta n_\theta)}$$

Finally, to have $\overline{U}[n_r, n_\theta] = \overline{U}[n_z]$, n_z has to be equal to: $n_z = int((n_r d_r \cos(-\pi + d_\theta n_\theta) - z_1) \times d_z)$, with $int()$ returning the closer integer. This can then be substitute in equation 12 to calculate the velocity perceived by the blade $\mathcal{U}$, as function of its angular position θ.

The quality of calculation of the angular velocity $\mathcal{U}(\theta)$ depends on the assumption that U is homogeneous along the y-axis. This assumption has been verified with previously acquired LDV measurements presented in [13]. A 2D cartography with 38 measurement points overall the turbine swept area has been carried out for the *Original grid* case and for a turbulent and shear case. Looking at the velocity cartographies, the mean velocity variations along the y-axis are small. Then, the velocity $\mathcal{U}(\theta)$ is calculated taking all the measurement points (over the entire rotor area) or just the points of the central line of the rotor and extruding it (as done in this paper). For the *Original grid* case, there is less than 1% difference between $\mathcal{U}(\theta)$ calculated from the central line and $\mathcal{U}(\theta)$ calculated from $\overline{U(y,z)}$. When the flow is sheared and turbulent, the difference is a bit larger: 2.5%. Thus, this assumption is correct and is responsible for less than 3% of error in the estimation of $\mathcal{U}(\theta)$.

The apparent velocities in the reference frame of the blade $\mathcal{U}(\theta)$ are presented in Figure 14. This figure shows that, for the three shear cases, the blade encounters different velocities while rotating. The velocity perceived by the blade $\mathcal{U}(\theta)$ is maximum for $\theta = 0$ rad, when the blade is at the top dead centre. For the *Panel 3* case, the velocity increases when the blade goes up, and decreases when the blade goes down. The difference between extreme values of $\mathcal{U}(\theta)$ is 0.09 m/s, which represents almost 10% of the mean value. However, results obtained for the *Panels 1* and *2* cases are more complex: some local peaks appears. A local minimum at $\theta = \pm\pi/2$ rad, i.e. when the blade is horizontally oriented, is observed for *Panel 1* and *Original grid*. At these positions, the entire surface of the blade is in the low-velocity area, observed in Figure 12. In the same way, a low-velocity zone appears around to $\theta = 0$ rad for the *Panel 2* case (see Figure 5). Consequently, the velocity perceived by the blade stays constant at $\mathcal{U} \simeq 1.02$ m/s, for $\theta \in [-\pi/2; \pi/2]$ rad.

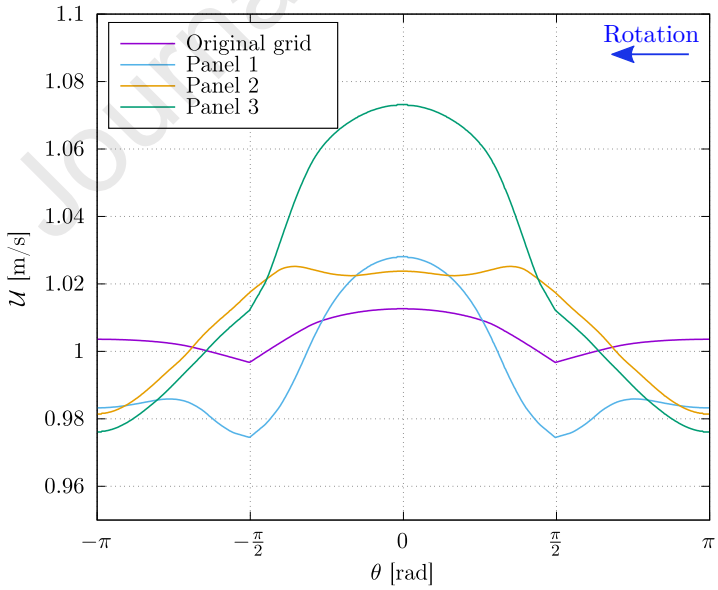

Figure 14: $\mathcal{U}(\theta)$ for blade 1 during its rotation, depending on θ. The direction of rotation is indicated by the blue arrow and corresponds to a negative direction.

To help the understanding of the velocity $\mathcal{U}$ evolution, two ideal cases are added. The first case is a perfectly constant velocity profile over the turbine height. The second case is a power-law presented in part 2.2. These both theoretical profiles with their corresponding measured profiles, i.e. *Original grid* and *Panel 3* cases respectively, are plotted in Figure 15.

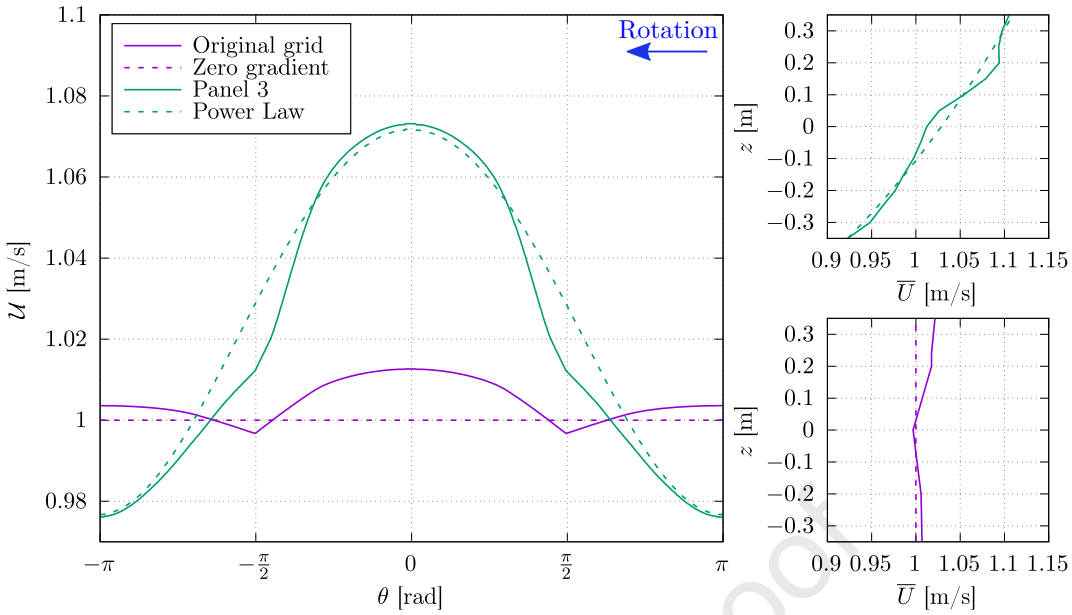

Figure 15: Superimposition of $\mathcal{U}(\theta)$ velocities computed from the *Original grid* and *Panel 3* cases and approximations (left). Approximated velocity profiles are also plotted (right). The direction of rotation is indicated by the blue arrow and corresponds to a negative direction.

When comparing $\mathcal{U}(\theta)$ in the case of the *Original grid* and a constant velocity profile (Figure 15), it appears that the *Original grid* creates small variations around $\theta = \pm\pi/2$ rad, which are explained by the low-velocity area around $z = 0$ m. For the *Panel 3* case, the power-law phase averaged velocity is very close to the real one. This approximation is relevant if we focus on the magnitude of variation during the blade rotation. The phenomenons occurring at $\theta = -\pi/2$ rad and $\theta = +\pi/2$ rad are however not present in the power-law variation, because at these angles ($z \approx 0$ m) the velocity profile of *Panel 3* differs from the power-law velocity profile.

The velocity perceived by the blade while rotating varies because there is a vertical gradient. In fact, $\mathcal{U}(\theta)$ is maximal when the blade is oriented towards the surface and minimal when it is oriented towards the bottom. This observation can be made for *Panel 1*, *2* and *3* cases, but there are other local extrema for the *Panel 1* and *2* cases.

3.3.2. Shear flow effect on blade loading

Figures 16 and 17 present the evolution of $\mathcal{F}_{x1}(\theta)$ and $\mathcal{U}^2(\theta)$ for the *Original grid* case and *Panel 1* to *3* cases. For the *Original grid* case, the amplitude of variation of $\mathcal{F}_{x1}(\theta)$ represents 2 N (3% of the mean value $\overline{F_{x1}}$). For the *Panel 3* case, the amplitude of variations of $\mathcal{F}_{x1}(\theta)$ is larger. It represents 10 N that corresponds to 17% of $\overline{F_{x1}}$. For both cases, the behaviour of the loads $\mathcal{F}_{x1}(\theta)$ follows the behaviour of the velocity $\mathcal{U}^2(\theta)$, but a varying phase delay is noticeable when the flow is sheared. For *Panel 3* case, this phase lag appears over the entire revolution and depends on the angular position θ of the studied blade.

Looking at *Panel 1* and *Panel 2* cases (Figure 17), the amplitude of variation of load and velocity are smaller than for *Panel 3*, representing approximatively 5 N for the load that corresponds to 9% of $\overline{F_{x1}}$. There are also noticeably less similarities between both quantities but they still have globally a similar behaviour. For the *Panel 1* case, a phase lag between the highest load and the highest velocity is observed as for the *Panel 3* case. A local minima of the velocity appears as well for $\theta = \pm\pi/2$ rad. For $\theta = -\pi/2$ rad, load phase average is synchronised with this velocity local minimum but it is not the case for $\theta = +\pi/2$ rad. A

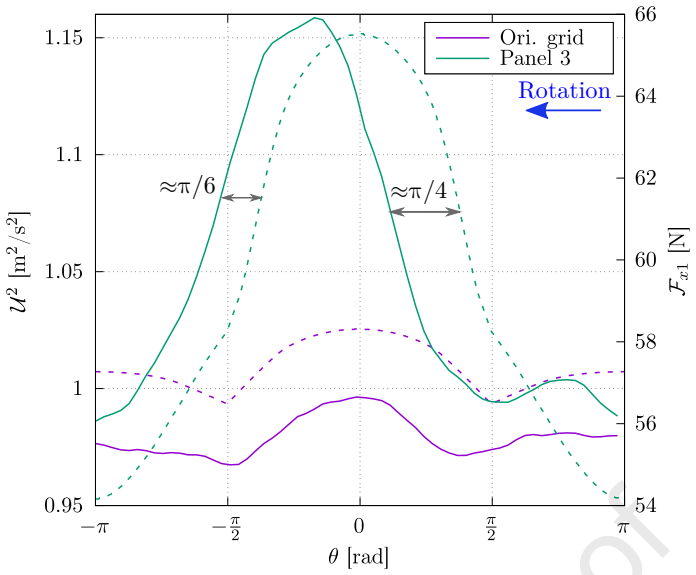

Figure 16: Load phase average on blade 1 $\mathcal{F}_{x1}(\theta)$ at $TSR = 4$ (*solid line*) compared with the squared velocity perceived by blade during its rotation $\mathcal{U}^2(\theta)$ (*dashed-line*) for *Original grid* and *Panel 3* cases. Horizontal grey arrows show how we estimate upward and downward phase lag. The direction of rotation is indicated by the blue arrow and corresponds to a negative direction.

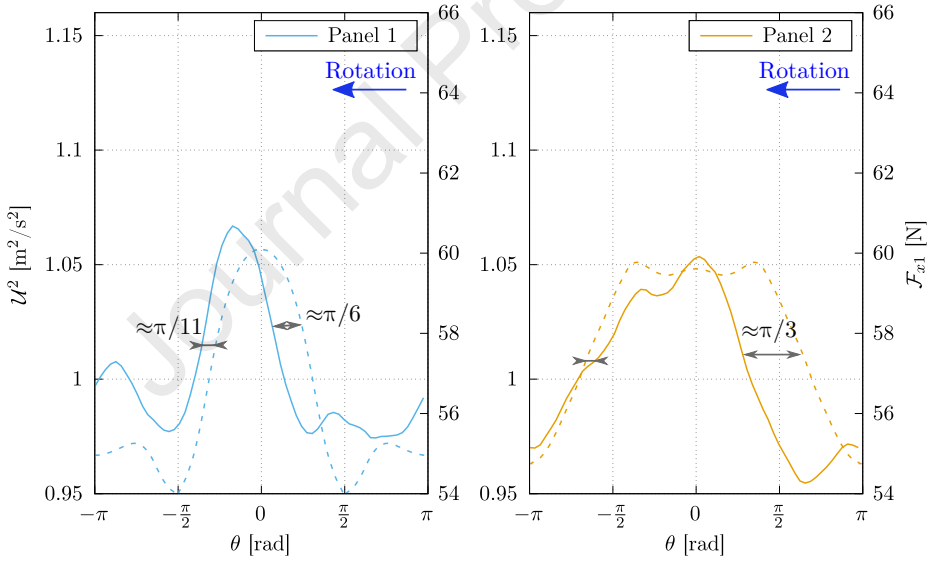

Figure 17: Load phase average on blade 1 $\mathcal{F}_x(\theta)$ at $TSR = 4$ (*solid line*) compared with the squared velocity seen by blade during its rotation $\mathcal{U}^2(\theta)$ (*dashed-line*) for *Panel 1* (left) and *Panel 2* (right) cases. Horizontal grey arrows show how we estimate upward and downward phase lag. The direction of rotation is indicated by the blue arrow and corresponds to a negative direction.

variable phase lag between both quantities appears as for *Panel 3*. For *Panel 2* case, the link between the load phase average and the squared velocity perceived by the blade is not as clear as for the three other cases. The main behaviour, with a maximum around $\theta \approx 0$ rad and a minimum around $\theta \approx \pm\pi$ rad, remains the same between load and squared velocity. For this case however, a global phase lag is difficult to identify as the shape of the two quantities differs.

These phase lags are then studied as a function of the blade movement. Upward and

downward phase lags are read in Figures 16 and 17 (horizontal grey arrows) and are summed up in table 4 for all *Panels* case. When $TSR = 4$, the turbine turns at $\omega = 11$ rad/s. So, the revolution period is 0.57 s. For all cases, the upward phase delay is larger than the downward phase delay. Depending on the case, the upward phase lag can represent up to $1/6^{\text{th}}$ of a revolution. The downward phase lag can represent up to $1/12^{\text{th}}$ of a revolution. This means that the load peak around $\theta = \pi/4$ rad is narrower (extend on a smaller range of θ) than the velocity peak centred around $\theta = 0$ rad.

Case	Upward phase delay	Downward phase delay
Panel 1	$\approx \pi/6$ rad $\Leftrightarrow$ 0.05 s	$\approx \pi/11$ rad $\Leftrightarrow$ 0.03 s
Panel 2	$\approx \pi/3$ rad $\Leftrightarrow$ 0.10 s	—
Panel 3	$\approx \pi/4$ rad $\Leftrightarrow$ 0.07 s	$\approx \pi/6$ rad $\Leftrightarrow$ 0.05 s

Table 4: Phase delay estimation from Figures 16 and 17

To go deeper into this phase average comparison, the cross-correlation coefficient is calculated between $\mathcal{F}_x(\theta)$ and $\mathcal{U}^2(\theta)$. For the sheared cases (*Panel 1*, *2* and *3*), a mean phase lag is read on the cross-correlation curve looking at the position of the maximum of correlation. These results are summed up in Table 5.

For the 3 cases, the maxima of cross-correlation coefficients are above 0.8. So, the phase average loads $\mathcal{F}_{x1}(\theta)$ are very similar to the phase squared velocities perceived by the blade $\mathcal{U}^2(\theta)$. The position of this maximum indicates the phase lag that enables the best similarity between these two compared quantities to be determined. The phase lag differs between the cases. These global phase lags, calculated from the cross-correlation, do not correspond to the upward and downward phase lag read on the Figures 16 and 17 (presented in table 4) as they are averaged over a revolution. For the *Panel 1* and *Panel 3* cases, a quite good correlation coefficient (≈ 0.9) is obtained between phase average loads and velocities. For the *Panel 2* case, even if velocity and load are less correlated, the signals stay strongly linked. This slightly lower cross-correlation coefficient is something expected looking at Figure 17, where the variations of the load are really different from the ones obtained for the velocity. In fact, the *Panel 2* velocity profile leads to more instationarities, explaining this lower correlation, due to its low velocity area at the rotor depth. These results show that the lag between $\mathcal{F}_{x1}(\theta)$ and $\mathcal{U}^2(\theta)$ depends on the shear of the velocity profile.

Case (at $TSR = 4$)	Maximum correlation coefficient ρ_M [-]	Lag at ρ_M [s] or [rad]
Panel 1	0.91	$0.3 \approx \pi/10$
Panel 2	0.81	$0.2 \approx \pi/15$
Panel 3	0.88	$0.4 \approx \pi/8$

Table 5: Angular lag and correlation coefficient between squared velocity and load on blade 1, obtained with a cross-correlation, in the three gradient cases at $TSR = 4$.

For a better understanding of this phase lag phenomenon, $\mathcal{F}_{x1}(\theta)$ is plotted for different TSR and is again compared to $\mathcal{U}^2(\theta)$ for *Panel 3* case (Figure 18). This figure shows that, until $TSR4$, the phase lag between $\mathcal{F}_{x1}(\theta)$ and $\mathcal{U}^2(\theta)$ increases when the rotational speed of the turbine increases. Also, when the rotational speed of the turbine increases, the load amplitude increases as well. This exactly corresponds to the thrust coefficient which increases with the TSR. Looking at what happens when the TSR is high, the turbine blade perceives larger load fluctuations at a higher frequency than for lower TSR. Consequently, these two phenomena add up so that it leads to worse the effects for the turbine blade, especially in a

material fatigue point of view. Theses conclusions are also observed for *Panel 1* case, but it is less obvious for the *Panel 2* case.

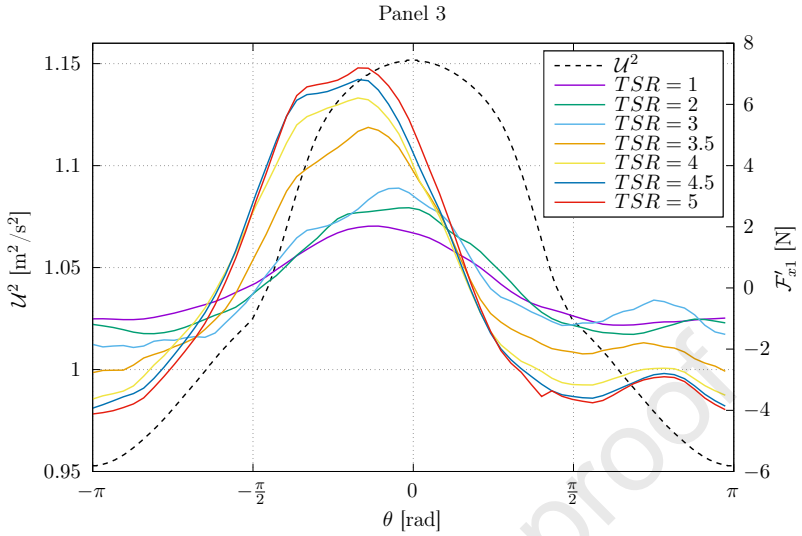

Figure 18: Load phase average on blade 1 $\mathcal{F}_x(\theta)$ (*solid line*) compared with the squared velocity seen by blade during its rotation $\mathcal{U}^2(\theta)$ (*dashed-line*) for *Panel 3* case.

The phase lag observed between $\mathcal{F}_{x1}(\theta)$ and $\mathcal{U}^2(\theta)$ depends in fact of many parameters. First of all, the velocity profile used to calculate the velocity perceived by the blade have been measured without the turbine in the flow. However, the presence of the turbine strongly modify and slow down the flow in front of it. This speed reduction is directly linked to the solidity of the rotor, so depends on the probability of occurrence of the blades and on the hub geometry. This is thus non homogeneous over the turbine rotor and modifies the incoming velocity profile [15, 8]. Moreover, the turbine drives a part of the surrounding flow in rotation. The flow is deflected from its original direction. This effect has been observed before both numerically and experimentally by Payne et al. [33] and Mason-Jones et al. [26]. The combination of these two effects is called the induction effect of the turbine [28].

In concrete more terms, this deflection of the flow by the turbine is certainly dependent on its rotational speed. In addition, the way the flow is slowed down by the solidity of the turbine depends on the incoming flow velocity profile and on the turbine rotational speed. Combining both effects, as they are interdependent, the shape of the velocity profile is homogeneously modified along the r-axis, thus along the y and z-axis. The velocity gradient wrap around the turbine in the rotation direction, toward $-\theta$. The velocity perceived by the blade is thus maximum a bit after $\theta = 0$ rad, so at $\theta < 0$ rad.

The induction effect of the turbine does not however fully explain:

- the evolution of the phase lag between $\mathcal{F}_{x1}(\theta)$ and $\mathcal{U}^2(\theta)$ versus θ,
- the difference between the θ range width where $\mathcal{F}_{x1}(\theta)$ and $\mathcal{U}^2(\theta)$ are high.

In fact, this reduction of the load peak width is likely due to a combination of the phenomena previously exposed and the fact that the blade's lift evolves during a revolution, due to the apparent velocity of the blade which changes during a revolution. This complex hydrodynamic phenomena are linked to the blade profile, the pitch and the turbine rotational speed and need further investigations to deeper understand these points.

4. Conclusion

The common generated flow in the IFREMER flume tank presents a low turbulence level, and a uniform vertical velocity profile over the tank height, excepted in the boundary layer. Three grid arrangements, named *Panels*, have been created to modify the vertical velocity profile of the tank, which have been characterized thanks to a 3C LDV system. *Panel 3* recreates a power-law profile ($\alpha = 4$), corresponding to the *in-situ* most sheared profiles. The two others, *Panels 1* and *2*, create more complex vertical velocity profiles as they present low-velocity at some specific heights. When looking at these velocity profiles on the area swept by the studied tidal turbine, these four cases are comparable in terms of mean velocity and turbulence intensity level. Thus, it enables the impact of shear incoming velocity profile on a horizontal-axis three-bladed tidal turbine to be studied.

The first step of the study is to evaluate the turbine global performance, using the power coefficient C_p. The calculation of the C_p requires to choose a characteristic velocity. This velocity is generally taken at the hub height, but in our case, velocity profiles are sheared over the rotor height. Thus, the velocity at the centre of the rotor is non-representative of the velocity perceived by the turbine. To overcome this problem, we use an equivalent velocity defined as the velocity averaged on the rotor height pondered by the area swept by blades. We show that, under this assumption, C_p is the same in the four cases, so the shape of the velocity profile does not impact the global turbine performance, providing the mean velocity remains similar in all cases, as it has been found for wind turbines.

Then, the focus is done on the horizontal load F_x on one blade. When the flow is sheared, the time evolution of F_x is partially periodic, and the amplitude of variations increases with the shear. The spectral analysis confirms that load is linked to the turbine rotation cycle as a peak appears at 1 to 3 times the rotation frequency of the turbine. Owing to this link, we calculate the phase average of F_x. We thus conclude that when the flow is sheared, $\mathcal{F}_x(\theta)$ presents a maximum between $\theta = -\pi/4$ rad and $\theta = 0$ rad which seems to be linked to an azimuthal velocity component due to the blade rotation.

Given that vertical velocity gradient has an impact on blade loading, we investigate the link between velocity perceived by a blade and its corresponding load. To do so, we calculate the velocity perceived by the blade at each rotation angle $\mathcal{U}(\theta)$ from the velocity profile coming from LDV measurements and knowing that $\overline{U(z)}$ is almost constant along the y-axis. First, we show that in the ideal case where the velocity profile follows a power-law, $\mathcal{U}(\theta)$ varies to reach a maximum at $\theta = 0$ rad, with a variation amplitude of 10%. Next, the phase average of load is compared with the squared velocity perceived by the blade, and it appears that the variation of these two quantities are very similar. Consequently, the cross-correlation coefficient between $\mathcal{F}_x(\theta)$ and $\mathcal{U}^2(\theta)$ is calculated. This coefficient reaches maximum value of 0.9 for a phase lag depending on the TSR and the incoming flow velocity profile. The link between the blade load and the squared velocity is thus established even if small differences are present. These differences are related to the turbine induction effects, which slow down the flow in front of the turbine in a inhomogeneous way and put it in rotation, and also to complex hydrodynamic phenomena around the blades.

This study is a first step to understand the effect of shear velocity profiles on tidal turbines. The long-term goal is to estimate, from *in-situ* measurements of the velocity profile, the blade load range and the load behaviour as function of the position of the turbine in the flow and of the angular position θ of the blades. To reach this goal, a wider range of conditions have to be tested and compared such as other incoming velocity profiles, with high turbulence level, changes in the solidity (number of blades) of the rotor, not only for horizontal axis tidal turbine. Further studies have to be conducted as well, looking at the changes of velocity profile

due to the induction of the turbine, using PIV or LDV measurement just in front of the rotor plane. Moreover, a fatigue study could be led to see how these very frequent and low intensity load fluctuations impact the durability of the turbine blade and make it more sensible to other external solicitations.

Acknowledgements

The research has received funding from the European Union Horizon 2020 Framework Program (H2020) for RealTide project under grant agreement no 727689. This project was partly financially supported by the French government, IFREMER and the region Hauts-de-France in the framework of the project CPER 2015-2020 MARCO

The authors would like to gratefully acknowledge Thomas Bacchetti and Jean-Valery Facq who involved in the experimental database generation and for their assistance and precious advices.

[1] Ahmed, U., Apsley, D.D., Afgan, I., Stallard, T., Stansby, P.K., 2017. Fluctuating loads on a tidal turbine due to velocity shear and turbulence: Comparison of CFD with field data. Renewable Energy 112, 235–246. URL: http://dx.doi.org/10.1016/j.renene.2017.05.048, doi:10.1016/j.renene.2017.05.048.

[2] Antoniou, I., Pedersen, S.M., Enevoldsen, P.B., 2009. Wind shear and uncertainties in power curve measurement and wind resources. Wind Engineering 33, 449–468. doi:10.1260/030952409790291208.

[3] Badshah, M., Badshah, S., VanZwieten, J., Jan, S., Amir, M., Malik, S.A., 2019. Coupled fluid-structure interaction modelling of loads variation and fatigue life of a full-scale tidal turbine under the effect of velocity profile. Energies 12. doi:10.3390/en12112217.

[4] Bandi, M.M., 2017. Spectrum of Wind Power Fluctuations. Physical Review Letters 118, 1–5. doi:10.1103/PhysRevLett.118.028301.

[5] Blackmore, T., Myers, L.E., Bahaj, A.S., 2016. Effects of turbulence on tidal turbines: Implications to performance, blade loads, and condition monitoring. International Journal of Marine Energy 14, 1–26. URL: http://dx.doi.org/10.1016/j.ijome.2016.04.017, doi:10.1016/j.ijome.2016.04.017.

[6] Bossuyt, J., Meneveau, C., Meyers, J., 2017. Wind farm power fluctuations and spatial sampling of turbulent boundary layers. Journal of Fluid Mechanics 823, 329–344. doi:10.1017/jfm.2017.328.

[7] Draycott, S., Payne, G., Steynor, J., Nambiar, A., Sellar, B., Venugopal, V., 2019. An experimental investigation into non-linear wave loading on horizontal axis tidal turbines. Journal of Fluids and Structures 84, 199–217. URL: https://doi.org/10.1016/j.jfluidstructs.2018.11.004, doi:10.1016/j.jfluidstructs.2018.11.004.

[8] Druault, P., Gaurier, B., Germain, G., 2022. Spatial integration effect on velocity spectrum: Towards an interpretation of the - 11/3 power law observed in the spectra of turbine outputs. Renewable Energy 181, 1062–1080. URL: https://www.sciencedirect.com/science/article/pii/S0960148121014014, doi:https://doi.org/10.1016/j.renene.2021.09.106.

[9] Druault, P., Germain, G., 2022. Prediction of the tidal turbine power fluctuations from the knowledge of incoming flow structures. Ocean Engineering 252, 111180. URL: https://www.sciencedirect.com/science/article/pii/S0029801822005856, doi:https://doi.org/10.1016/j.oceaneng.2022.111180.

[10] Ebdon, T., Allmark, M., O'Doherty, D.M., Mason-Jones, A., O'Doherty, T., Germain, G., Gaurier, B., 2020. The impact of turbulence and turbine operating condition on the wakes of tidal turbines. Renewable Energy URL: https://linkinghub.elsevier.com/retrieve/pii/S0960148120318085, doi:10.1016/j.renene.2020.11.065.

[11] Furgerot, L., Du Bois, P.B., Méar, Y., Morillon, M., Poizot, E., Bennis, A.C., 2018. Velocity profile variability at a tidal-stream energy site (Alderney Race, France): From short (second) to yearly time scales. 2018 OCEANS - MTS/IEEE Kobe Techno-Oceans, OCEANS - Kobe 2018 , 1–8doi:10.1109/OCEANSKOBE.2018.8559326.

[12] Furgerot, L., Sentchev, A., Bailly du Bois, P., Lopez, G., Morillon, M., Poizot, E., Méar, Y., Bennis, A.C., 2020. One year of measurements in Alderney Race: preliminary results from database analysis. Philosophical transactions. Series A, Mathematical, physical, and engineering sciences 378, 20190625. doi:10.1098/rsta.2019.0625.

[13] Gaurier, B., 2020. Étude expérimentale des performances d'une hydrolienne, soumise aux effets de la turbulence et de l'interaction houle-courant. Ph.D. thesis. Normandie Université. URL: https://tel.archives-ouvertes.fr/tel-03030615.

[14] Gaurier, B., Davies, P., Deuff, A., Germain, G., 2013. Flume tank characterization of marine current turbine blade behaviour under current and wave loading. Renewable Energy 59, 1–12. URL: http://dx.doi.org/10.1016/j.renene.2013.02.026, doi:10.1016/j.renene.2013.02.026.

[15] Gaurier, B., Druault, P., Ikhennicheu, M., Germain, G., 2020a. Experimental analysis of the shear flow effect on tidal turbine blade root force from three-dimensional mean flow reconstruction. Philosophical transactions. Series A, Mathematical, physical, and engineering sciences 378, 20200001. doi:10.1098/rsta.2020.0001.

[16] Gaurier, B., Germain, G., Facq, J.V., Bacchetti, T., 2018. Wave and current flume tank of IFREMER at Boulogne-sur-mer. Description of the facility and its equipment. Technical Report. doi:10.13155/58163.

[17] Gaurier, B., Germain, G., Facq, J.V., Johnstone, C.M., Grant, A.D., Day, A.H., Nixon, E., Di Felice, F., Costanzo, M., 2015. Tidal energy "Round Robin" tests comparisons between towing tank and circulating tank results. International Journal of Marine Energy 12, 87–109. doi:10.1016/j.ijome.2015.05.005.

[18] Gaurier, B., Ikhennicheu, M., Germain, G., Druault, P., 2020b. Experimental study of bathymetry generated turbulence on tidal turbine behaviour. Renewable Energy 156, 1158–1170. doi:10.1016/j.renene.2020.04.102.

[19] Gaurier, B., Ordonez-Sanchez, S.E., Facq, J.V., Germain, G., Johnstone, C.M., Martinez, R., Salvatore, F., Santic, I., Davey, T., Old, C., Sellar, B.G., 2020c. MaRINET2 tidal energy round robin tests-performance comparison of a horizontal axis turbine subjected to combined wave and current conditions. Journal of Marine Science and Engineering 8. doi:10.3390/JMSE8060463.

[20] Gooch, S., Thomson, J., Polagye, B., Meggitt, D., 2009. Site characterization for tidal power. MTS/IEEE Biloxi - Marine Technology for Our Future: Global and Local Challenges, OCEANS 2009 doi:10.23919/oceans.2009.5422134.

[21] IEC TS 62600-200:2013, 2013. Part 200: Electricity producing tidal energy converters - Power performance assessment, in: INTERNATIONAL, ELECTROTECHNICAL, COMMISSION (Eds.), Marine energy - Wave, tidal and other water current converters, p. 51. URL: https://webstore.iec.ch/publication/7242.

[22] Ke, S., Wen-Quan, W., Yan, Y., 2020. The hydrodynamic performance of a tidal-stream turbine in shear flow. Ocean Engineering 199, 107035. doi:10.1016/j.oceaneng.2020.107035.

[23] Lewis, M.J., Neill, S.P., Robins, P.E., Hashemi, M.R., Ward, S.L., 2017. Characteristics of the velocity profile at tidal-stream energy sites. Renewable Energy 114, 258–272. URL: http://dx.doi.org/10.1016/j.renene.2017.03.096, doi:10.1016/j.renene.2017.03.096.

[24] Li, L., Liu, Y., Yuan, Z., Gao, Y., 2018. Wind field effect on the power generation and aerodynamic performance of offshore floating wind turbines. Energy 157, 379–390. doi:10.1016/j.energy.2018.05.183.

[25] Magnier, M., Germain, G., Gaurier, B., Druault, P., 2021. Velocity profile effects on a bottom-mounted square cylinder wake and load variations, in: Proceedings of the 14th European Wave and Tidal Energy Conference 5-9th Sept 2021, Plymouth, UK, pp. 2249–1–10. URL: https://archimer.ifremer.fr/doc/00721/83291/.

[26] Mason-Jones, A., O'Doherty, D.M., Morris, C.E., O'Doherty, T., 2013. Influence of a velocity profile & support structure on tidal stream turbine performance. Renewable Energy 52, 23–30. doi:10.1016/j.renene.2012.10.022.

[27] Mercier, P., Guillou, S., 2021. The impact of the seabed morphology on turbulence generation in a strong tidal stream. Physics of Fluids 33. doi:10.1063/5.0047791.

[28] Meyer Forsting, A.R., 2017. Modelling Wind Turbine Inflow: The Induction Zone. Ph.D. thesis. doi:10.11581/DTU:00000022.

[29] Milne, I.A., Sharma, R.N., Flay, R.G., Bickerton, S., 2013. Characteristics of the turbulence in the flow at a tidal stream power site. Philosophical Transactions of the Royal Society A: Mathematical, Physical and Engineering Sciences 371. doi:10.1098/rsta.2012.0196.

[30] Moreau, M., Germain, G., Maurice, G., Richard, A., Coquet, R., 2021. HydroQuest : Feedback from Paimpol-Bréhat and validation of the design method, in: Proceedings of the 14th European Wave and Tidal Energy Conference 5-9th Sept 2021, Plymouth, UK, pp. 2229–1–8.

[31] Mycek, P., Gaurier, B., Germain, G., Pinon, G., Rivoalen, E., 2014. Experimental study of the turbulence intensity effects on marine current turbines behaviour. Part I: One single turbine. Renewable Energy 66, 729–746. doi:10.1016/j.renene.2013.12.036.

[32] Owen, P.R., Zienkiewicz, H.K., 1957. The production of uniform shear flow in a wind tunnel. Journal of Fluid Mechanics 2, 521–531. URL: https://www.cambridge.org/core/journals/journal-of-fluid-mechanics/

article/abs/production-of-uniform-shear-flow-in-a-wind-tunnel/68D271C5CBEADADC111B5C0803111A9B, doi:10.1017/S0022112057000336.

[33] Payne, G.S., Stallard, T., Martinez, R., Bruce, T., 2018. Variation of loads on a three-bladed horizontal axis tidal turbine with frequency and blade position. Journal of Fluids and Structures 83, 156–170. doi:10.1016/j.jfluidstructs.2018.08.010.

[34] Sentchev, A., Nguyen, T.D., Furgerot, L., Bailly du Bois, P., 2020. Underway velocity measurements in the Alderney Race: towards a three-dimensional representation of tidal motions. Philosophical transactions. Series A, Mathematical, physical, and engineering sciences 378, 20190491. doi:10.1098/rsta.2019.0491.

[35] Sezer-Uzol, N., Uzol, O., 2013. Effect of steady and transient wind shear on the wake structure and performance of a horizontal axis wind turbine rotor. Wind Energy 16, 1–17. doi:10.1002/we.514.

[36] Shen, X., Zhu, X., Du, Z., 2011. Wind turbine aerodynamics and loads control in wind shear flow. Energy 36, 1424–1434. doi:10.1016/j.energy.2011.01.028.

[37] Thiébaut, M., Filipot, J.F., Maisondieu, C., Damblans, G., Jochum, C., Kilcher, L.F., Guillou, S., 2020. Characterization of the vertical evolution of the three-dimensional turbulence for fatigue design of tidal turbines. Philosophical transactions. Series A, Mathematical, physical, and engineering sciences 378, 20190495. doi:10.1098/rsta.2019.0495.

[38] Thiébaut, M., Sentchev, A., 2017. Asymmetry of tidal currents off the W.Brittany coast and assessment of tidal energy resource around the Ushant Island. Renewable Energy 105, 735–747. doi:10.1016/j.renene.2016.12.082.

[39] Thomson, J., Polagye, B., Durgesh, V., Richmond, M.C., 2012. Measurements of turbulence at two tidal energy sites in puget sound, WA. IEEE Journal of Oceanic Engineering 37, 363–374. doi:10.1109/JOE.2012.2191656.

[40] Vinod, A., Han, C., Banerjee, A., 2021. Tidal turbine performance and near-wake characteristics in a sheared turbulent inflow. Renewable Energy 175, 840–852. URL: https://www.sciencedirect.com/science/article/pii/S0960148121007023, doi:https://doi.org/10.1016/j.renene.2021.05.026.

[41] Wagner, R., Antoniou, I., Pedersen, S.M., Courtney, M.S., Jørgensen, H.E., 2009. The influence of the wind speed profile on wind turbine performance measurements. Wind Energy 12, 348–362. doi:10.1002/we.297.

[42] Wagner, R., Courtney, M., Lindelöw-Marsden, P., Gottschall, J., 2011. Accounting for the speed shear in wind turbine power performance measurement. Wind Energy 14, 933–1004. doi:10.1002/we.509.

Declaration of interests

☒ The authors declare that they have no known competing financial interests or personal relationships that could have appeared to influence the work reported in this paper.

☐The authors declare the following financial interests/personal relationships which may be considered as potential competing interests: